Cell-resolved blood flow simulations of saccular aneurysms: effects of pulsatility and aspect ratio

Czaja, B.; Závodszky, G.; Azizi Tarksalooyeh, V.; Hoekstra, A.G.

DOI
10.1098/rsif.2018.0485

Publication date
2018

Document Version
Final published version

Published in
Journal of the Royal Society Interface

INTERFACE

rsif.royalsocietypublishing.org

Research

Cite this article: Czaja B, Závodszky G, Azizi Tarksalooyeh V, Hoekstra AG. 2018 Cell-resolved blood flow simulations of saccular aneurysms: effects of pulsatility and aspect ratio. *J. R. Soc. Interface* **15**: 20180485. http://dx.doi.org/10.1098/rsif.2018.0485

Received: 28 June 2018
Accepted: 28 August 2018

Subject Category:
Life Sciences – Engineering interface

Subject Areas:
biomechanics, biophysics, biomedical engineering

Keywords:
red blood cells, platelets, aneurysm, pulsatile flow, blood rheology, transport phenomena

Author for correspondence:
B. Czaja
e-mail: B.E.Czaja@uva.nl

Electronic supplementary material is available online at https://dx.doi.org/10.6084/m9.figshare.c.4221647.

THE ROYAL SOCIETY PUBLISHING

Cell-resolved blood flow simulations of saccular aneurysms: effects of pulsatility and aspect ratio

B. Czaja[1], G. Závodszky[1,2], V. Azizi Tarksalooyeh[1] and A. G. Hoekstra[1,3]

[1]Computational Science Lab, University of Amsterdam, Amsterdam, The Netherlands
[2]Department of Hydrodynamic Systems, Budapest University of Technology and Economics, Budapest, Hungary
[3]ITMO University, St Petersburg, Russia

BC, 0000-0003-1140-5698; AGH, 0000-0002-3955-2449

We study the effect of pulsatile flow on the transport of red blood cells (RBCs) and platelets into aneurysm geometries with varying dome-to-neck aspect ratios (AR). We use a validated two-dimensional lattice Boltzmann model for blood plasma with a discrete element method for both RBCs and platelets coupled by the immersed boundary method. Flow velocities and vessel diameters were matched with measurements of cerebral perforating arteries and flow was driven by a synthetic heartbeat curve typical for such vessel sizes. We observe a flow regime change as the aspect ratio increases from a momentum-driven regime in the small aspect ratio to a shear-driven regime in the larger aspect ratios. In the small aspect ratio case, we see the development of a re-circulation zone that exhibits a layering of high (greater than or equal to 7 s) and low (less than 7 s) residence cells. In the shear-driven regime, we see high and low residence cells well mixed, with an increasing population of cells that are trapped inside the aneurysm as the aspect ratio increases. In all cases, we observe aneurysms that are platelet-rich and red blood cell-poor when compared with their respective parental vessel populations. Pulsatility also plays a role in the small aspect ratio as we observe a smaller population of older trapped cells along the aneurysm wall in the pulsatile case when compared with a steady flow case. Pulsatility does not have a significant effect in shear-driven regime aspect ratios.

1. Introduction

Cerebral aneurysms have been estimated to occur in 1–5% of the general population [1], and the chance for rupture has been estimated to occur in 6–8 per 100 000 people [2]. Thrombosis is one of the body's natural responses to heal damaged vessel walls and has been found to reduce the probability of rupture [3] by occluding the aneurysm sac. Autopsy studies reveal that about 9–13% of intra-cranial aneurysms had a formed thrombus [4]. However, the formation of a thrombus may also have detrimental health effects, i.e. a blood clot breaking off from a formed thrombus to travel downstream to cause an ischaemic stroke. The full mechanism of thrombus formation inside cerebral aneurysms depends on the size and location of the aneurysms, blood flow patterns inside the aneurysm, as well as biochemical factors. Understanding these processes is crucial for treatment procedures for cerebral aneurysms.

Macroscopic computational fluid dynamic (CFD) simulations, where whole blood is represented as a continuous fluid, are a powerful tool for studying blood flow in cerebral aneurysms. They can incorporate patient-specific geometries [5–8], study the flow patterns inside an aneurysm [9,10] and assess the risk of rupture based on location and geometry [11] at a relatively low computational cost. In order to save computational overheads, blood is usually assumed to be an incompressible Newtonian fluid. This has been proved to be a reasonable approximation for flow in large vessels but may not be applicable in aneurysms due to low shear regions where the non-Newtonian behaviour of

blood becomes important [12]. Continuous fluid simulations, using non-Newtonian viscosity models, have been employed to study haemodynamics in cerebral aneurysms [13–16].

The lattice Boltzmann method (LBM) [17,18] can be applied to study continuous fluid dynamics and historically has been used for CFDs. A prominent continuous LBM model for haemodynamics has been proposed by Ouared & Chopard [19] to model the initiation and growth of a thrombus in a cerebral aneurysm. In this model, below a certain shear rate the probability of adhesion of platelets to an aneurysm wall is high and here a thrombus is likely to form [20,21]. In this method, platelets are modelled as point particles tracing flow lines as passive scalars [22], which was able to reproduce the shape and volume of formed thrombi in patient-specific aneurysms [23]. This method also revealed through a cross-sectional study of 21 patients an association between spontaneous thrombosis and aneurysm dome to neck aspect ratio [24].

Cell-resolved computational models [25–28] are very useful to blood flow modelling as they can resolve the mechanics of individual red blood cells (RBCs) and the resulting non-Newtonian flow properties of whole blood as a suspension of RBCs. However, these models are computationally expensive and as a result are usually restricted to study systems less than or equal to 150 μm in size and less than or equal to 1 s in time. In this paper, we apply a two-dimensional cell-resolved blood flow model to study flow in cerebral aneurysms on the time and spatial scales achievable by continuous CFD models. We provide time-dependent (systolic) cell-resolved blood flow simulations to study the transport of deformable RBCs and quasi-rigid platelets into, and emerging flow properties of, two-dimensional saccular aneurysms. Here, we focus on flow proprieties and cell locations inside the aneurysms, as we can resolve the non-Newtonian behaviour of whole blood as a result of the suspension of deformable RBCs. We extend upon a previous work of two-dimensional cell-resolved simulations of sidewall aneurysms [29] by providing pulsatile flow and cell residence times. We also extend the physical simulated time from 0.2 s to 7.7 s, and the vessel diameter from 100 μm to 260 μm and the aneurysm diameter from 250 μm to 800 μm. To our knowledge, this is the first cell-resolved study to include a full heart pulse, here we simulate 10 heart cycles in total. Residence times are computed at each time step for each cell allowing us to locate where and how long cells spend in the aneurysms.

In §2, we describe the blood flow model used, the geometries, the boundary conditions, the initializations of RBCs and platelets in the domains, and the computational resources used. In §3, we show the results of our simulations; the emerging flow patterns in the aneurysms, the cell populations in the aneurysms under both pulsatile and steady flow, as well as the locations and age of the cells in the aneurysms. In §4, we provide conclusions and a discussion of our findings.

2. Methods

We use a validated [30] two-dimensional cell-resolved LBM for the blood plasma with a discrete element method (DEM) for both RBCs and platelets which is connected to the plasma via the immersed boundary method [31]. The material model for the RBCs consists of 26 Lagrangian surface points (LSP) where each LSP is connected together through a force network. The DEM force network is a superposition of a Hookean spring force connecting neighbouring LSPs, a bending force to add bending resistance to the springs, an area conservation force to ensure that cells maintain their shape, and a repulsion force to mitigate cell–cell interactions which prevents cells membranes from overlapping. The resulting equilibrium shape from the DEM model is a biconcave RBC that is 8 μm in diameter. Semi-rigid platelets consist of eight LSPs that result in a disc shape with a diameter 2 μm. Lattice Boltzmann fluid nodes have a spatial resolution of $dx = 1$ μm which sufficiently resolves the rheology of the suspension of RBCs. Details of the revalidation of this model are shown in appendix A.1.

2.1. Domain geometry

Saccular aneurysms generally appear on the sidewall of a curved vessel or at a bifurcation point [32]. Aneurysms with larger neck sizes have been found to be exposed to higher shear stresses than those with smaller necks [33]. And aneurysms with a dome-to-neck aspect ratio greater than 1.6 have been correlated with a greater risk of rupture [34]. A sidewall aneurysm with no branching vessels is a simple geometry that we can probe in two dimensions that will allows us to isolate the effects of aspect ratio. Dome-to-neck aspect ratio is measured as the height of the dome over the width of the neck of the aneurysm.

$$\mathrm{AR} = \frac{h}{d_\mathrm{h}}. \tag{2.1}$$

The height of the dome is measured from the aneurysm wall opposite to the neck to the entrance of the neck (figure 1*a*). We place sidewall saccular cerebral aneurysms on the edge of a 90° curved vessel and probe varying aneurysm dome-to-neck aspect ratios of 1, 2, 3 and 4. Parental vessels are 260 μm in diameter with aneurysms diameters of approximately 800 μm.

2.2. Boundary conditions

A schematic of the computational domain is shown in figure 1*a*, highlighting the boundary conditions employed. We adopt the inlet–outlet boundary conditions of [35], where the macroscopic velocity from the periodic 'pre-inlet' domain is copied to the first row of the lattice Boltzmann fluid nodes of the flow domain with the help of the Zou–He [36] boundary condition. Flow in the periodic domain is driven via a time-varying body force $\vec{F}(t)$ which is directly applied to the lattice Boltzmann fluid cells [18]. This is a valid approximation because the time steps are much smaller than the timescale on which the pulse wave changes.

The proximity of the inlet and outlet boundary conditions can perturb the flow present in the aneurysm geometry [13,37,38]. As we use a periodic pre-inlet domain, the inlet boundary condition can be seen as significantly far away from the aneurysm entrance and therefore does not introduce potentially perturbing flow into the aneurysm geometry. The outlet is located 460 μm after the aneurysm neck. We prescribe a constant density at the outlet and observe that there is no significant change in the velocity profile near the outlet. This is in agreement with a previous study finding that the outflow condition only has a localized effect on the flow pattern [38]. We estimate that the outlet implementation has a significant effect on the flow profile up to 30 μm from the outlet. Additionally, the Reynolds numbers in this study range from 33 at systole and eight at diastole which are relatively low and therefore flow within the parental vessel is laminar.

Fluid–structure interaction simulations have shown that including the elasticity of the arterial walls does effect the flow dynamics, especially in larger arteries like the aorta [39–41]. Vessel deformability is out of the scope of this study; therefore, we assume that vessel walls in our simulations are rigid. Vessels of the sizes considered in this study are much less compliant than in larger arteries [42,43], and therefore we believe this a reasonable modelling choice. We prescribe a bounce-back boundary condition at the vessel wall.

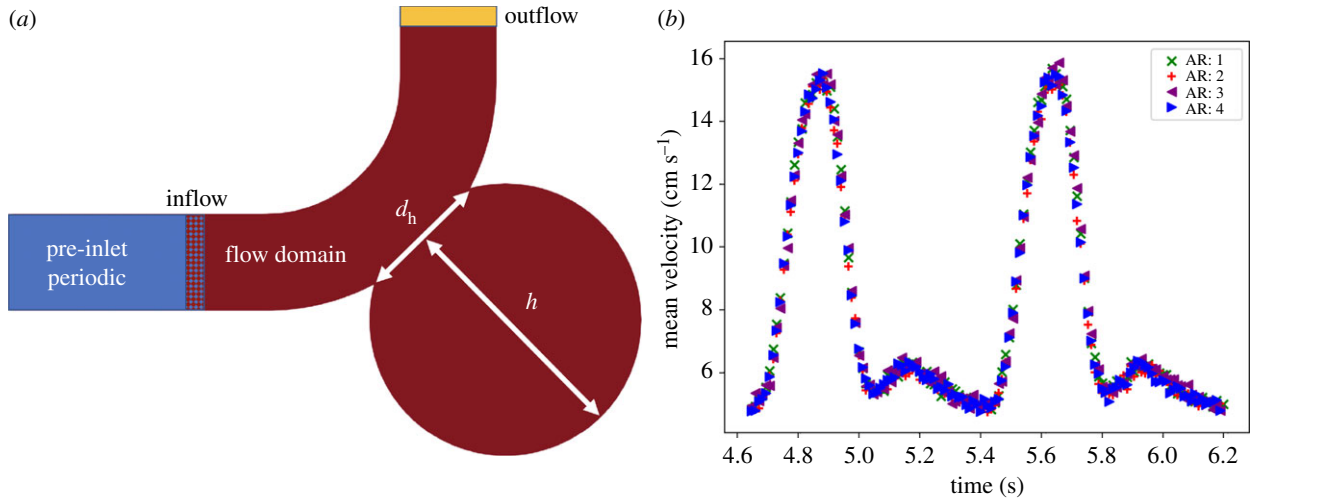

Figure 1. (*a*) The curved vessel with circular aneurysm geometry. Periodic pre-inlet domain shown in blue, flow domain shown in red and outlet/outflow region shown in yellow. Dome-to-neck aspect ratio is the ratio of dome height d_h to neck width h. (*b*) The mean parental velocity over two heart cycles computed in each of the aspect ratio geometries. (Online version in colour.)

The simulations presented in this paper run for approximately 8 s in real time, which is $O(10^7)$ lattice Boltzmann time steps. With such long run times, we rely on these inlet–outlet boundary conditions as the cell distributions of the parental vessel will change if only using periodic boundary conditions. With this method, cells are copied from the periodic domain to the flow domain as they wrap around the periodic domain, and are deleted at the outlet of the flow domain. This allows us to properly populate the flow domain with an endless supply of cells from the periodic domain.

2.3. Pulse wave

We tested the accuracy of these boundary conditions by driving the periodic domain with a sinusoidal time varying body force and compared the resulting flow profile recovered from the flow domain with the theoretical flow profile predicted by Womersley [44]. In this test, the fluid is continuous (without cells) with a dynamic plasma viscosity of $\mu = 1.29$ mPa and is driven in a straight pipe, so we can isolate the effect of the boundary conditions to compare to the Womersley solution. The Reynolds number of such a flow is $Re = 15.38$ with a heart rate of 1 beat per second which results in a Womersley number of $\alpha = 0.4$. We find a relative error between theory and computed flow profiles of less than or equal to 0.1% over five heart cycles. This is in good agreement with a previous study of pulsatile flow in two dimensions using the LBM which reports a relative error of 0.85%, using periodic boundary conditions [45]. We anticipate that our error is smaller as we drive the flow with lower Reynolds and Womersley numbers.

Systolic flow in the aneurysm geometries is driven by a time-dependent body force, applied to the pre-inlet domain, resulting from a synthetic pulse wave signal [8] that has similar properties to a cardiac pulse wave found in real cerebral aneurysms. The computed mean parental vessel velocity was set to match the mean flow velocities measured in cerebral perforating arteries of similar sizes [46]. The computed mean parental vessel velocity, resulting from the synthetic pulse wave, in each of the geometries has an average over all heart beats of 7.81 ± 0.06 cm s^{-1}, with an average peak of 15.7 ± 0.2 cm s^{-1} at systole, and an average minimum of 4.67 ± 0.09 cm s^{-1} at diastole. The mean parental velocity is computed by averaging all velocities within a cross-section across the width the parental vessel. Shown in figure 1*b* is the computed mean velocity of the parental vessel over two heart cycles for all aspect ratios. The system reaches an equilibrium velocity state within the first pulse. The initial transients of the system vanish within the first pulse.

2.4. Initial conditions

We populated the flow domains with either an initial state filled with both RBCs and platelets or empty with only LBM fluid nodes. In the filled case, the entire domain, pre-inlet and flow domain, is populated uniformly with cells. In the empty case, only the pre-inlet domain is populated uniformly with cells which are then washed into the flow domain as the simulation progresses. Each geometry was populated to an initial tube haematocrit of 42%, which represents normal adult male physiological values [47]. Following the empirical relationship between the tube diameter and tube haematocrit, this corresponds to a discharge or tank haematocrit of 43%. The higher haematocrit of an adult male was chosen as we can simulate higher haematocrits in two dimensions efficiently. We initialize with a platelet to RBC count ratio of $\frac{1}{10}$ [48] which results in a platelet volume fraction of $C_{\mathrm{plt}} = 0.0021$ in the parental vessel. We define the platelet volume fraction C_{plt} as the volume fraction of platelets measured at a specific location $\tilde{C}_{\mathrm{plt}}$ normalized to the arithmetic mean of the parental vessel platelet volume fraction $\bar{C}_{\mathrm{plt}}$, i.e. $C_{\mathrm{plt}} = \tilde{C}_{\mathrm{plt}}/\bar{C}_{\mathrm{plt}}$. The two initializations of the flow domain present different aneurysm velocities, see figure 2, and aneurysm cell volume fractions (figure 3). Further details of the initializations are discussed in §3.

3. Results

3.1. Empty initialization

In figure 3, we observe in aspect ratio 1 (AR1) that the system is filled within the first heart beat and reaches an quasi-equilibrium haematocrit state of 0.34 ± 0.003. Heat maps of the cell volume fractions are shown over the last heart beat in the left column of figure 4. As the aspect ratio increases (AR2, AR3, AR4), we observe a shear-driven regime where flow in the aneurysm is sheared at the neck which creates a circular flow inside aneurysm. Haematocrits of these geometries do not reach an equilibrium value during the simulation time. Final haematocrits, reported in table 1, are significantly lower than the parental vessel haematocrits. Flow of cells into these geometries is qualitatively similar to observations made in *in vitro* experiments of spherical sidewall aneurysms [49].

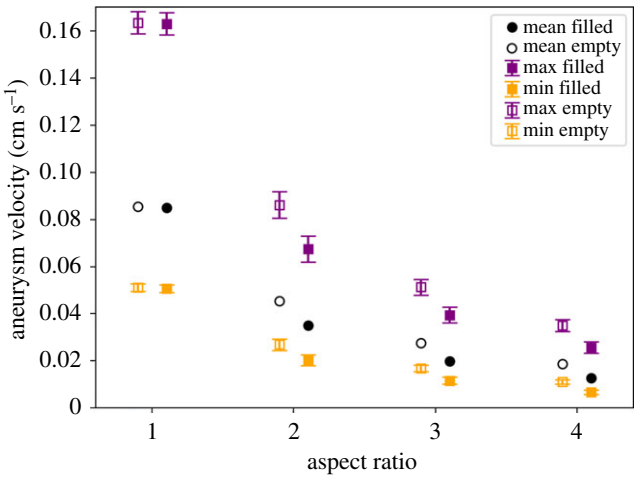

Figure 2. Average of the velocity magnitude inside the aneurysms over the last nine heart cycles as a function of aspect ratio. Black dots are the overall mean velocity, purple squares are the average maximum (systole) velocity and orange boxes are the average minimum (diastole) velocity from the final nine heart cycles. Error bars show the standard error of the mean for each averaged value. Filled markers denote the filled initialization and empty denotes empty flow domain initializations. (Online version in colour.)

Cells in this regime that are washed into the aneurysm at the neck fill up the aneurysm along the walls, and they circle inside as they transit towards the centre of the aneurysm, see the right three columns of figure 4. Average aneurysm velocity magnitudes in the empty initialization are 0.085 cm s^{-1} in AR1, 0.045 cm s^{-1} in AR2, 0.027 cm s^{-1} in AR3 and 0.018 cm s^{-1} in AR4. These velocities are averaged over the final nine heart cycles and are shown in figure 2.

3.2. Filled initialization

In the filled initialization, we observe similar flow regimes as in the empty initialization. AR1 is momentum driven and reaches an equilibrium haematocrit of 0.35 ± 0.03 within the first pulse. While in the AR2, AR3 and AR4 geometries are shear driven and do not seem to reach an equilibrium haematocrit after 10 pulses. This is highlighted in the time series of the aneurysm haematocrits, shown in figure 3*a*, of AR2 (red dot dashed line), AR3 (purple dashed line) and AR4 (blue dotted line). Haematocrits in all aspect ratios are less than the parental vessel haematocrits. We observe a high haematocrit old cell population that increases along the aneurysm wall as aspect ratio increases (figure 4). Velocities in the aneurysms of the filled initialization exhibit lower velocities compared to the empty case, shown in figure 2, which are averaged over the final nine pulses. Aneurysms velocity values with the filled initialization are 0.085 cm s^{-1} in AR1, 0.035 cm s^{-1} in AR2, 0.019 cm s^{-1} in AR3 and 0.012 cm s^{-1} in AR4. We attribute the decrease in velocity to an increase in the suspension viscosity in the aneurysms due to a larger population of cells in the filled initialization. The effect is present in the peak, mean and minimum of each pulse, which is displayed in figure 2.

In both initializations, aneurysm haematocrits are depleted and platelet volume fractions are enriched compared to their parental vessel populations. This is evident across all aspect ratios. This is interestingly also evident in the recirculation zone of AR1, where the recirculation zone is depleted of red blood cells and enriched with platelets. We extended the AR2 empty simulation to 16.5 s, to investigate if the system would reach an equilibrium aneurysm haematocrit. We observe that the total haematocrit follows an inverse exponential growth $\propto \exp^{-2.17}$ and reaches a haematocrit of 0.25 at 16.5 s (approx. 21 heart cycles). This slow growth of haematocrit can be attributed to the diffusive nature of RBCs towards the centre. This diffusion of RBCs slows down closer towards the centre as shear rates decrease from the aneurysm wall to the centre of the aneurysm sac.

3.3. Effect of aspect ratio

We observe that the average aneurysm velocity decreases as the aspect ratio increases, as shown in figure 2. This effect is apparent across all aspect ratios and initializations. There is also a two orders of magnitude velocity decrease inside the aneurysm compared to the parental vessel. As an example in AR1, we observe a mean flow velocity over an entire heart cycle of 7.8 cm s^{-1}, compared to an average velocity of 0.068 cm s^{-1} inside the aneurysm.

We find a flow regime change from momentum driven in AR1 to a shear-driven regime in AR2, AR3 and AR4. Flow stream lines over one heart cycle are shown in figure 5, for both momentum (AR1) and shear-driven (AR3) regimes. In the AR1 case, we see a re-circulation zone that is sustained over an entire heart cycle, see the second row of figure 5. The location of the vortex varies through one heart cycle, and in some instances sub-vortices also develop along the recirculation zone. We also find regions of flow reversal along the wall, but it should be noted the magnitude of these velocities is very small and occurs in high haematocrit regions. In the shear-driven regime, we do not observe any recirculation zone or sub-vortices. There exists one constant vortex throughout the entire heart cycle that keeps a constant position.

Over all aspect ratios, we observe that the aneurysms are red blood cell-poor and platelet-rich with respect to each cells vessel volume fraction. This is shown as a time series in figure 3 and in the heat maps in figure 4, with the specific end state values reported in table 1. We attribute the richness of platelets in the aneurysms to platelet margination observed in our simulations, shown in figure 8*c*. Margination of platelets has been observed in multiple *in vitro* studies [50,51] and in other two-dimensional simulations of cell-resolved blood flow [29,35,52]. Platelets are already at higher volume fraction at the vessel wall before they encounter the entrance of the aneurysm, so they preferentially enter the sac. The depletion of RBCs in the aneurysm we attribute to the existence of a cell free layer, shown in figure 8*b*, in the parental vessel. The cell free layer restrains RBCs from being washed into the aneurysm as there is a lacking of RBCs along the vessel wall before the entrance of the aneurysm.

We observe an increase in high resident cells as aspect ratio increases, with a large step increase going from the momentum to the shear-driven regime. This effect is highlighted in figure 6 where we show the ratio of high residence cells (residence times greater than or equal to 7 s denoted N_{old}) to the total number of cells present (denoted N) in the aneurysms over all aspect ratios and initializations. The percentage of cells with residence times greater than or equal to 7 s is 2.3% in AR1, 61.5% in AR2, 74.8% in AR3, and 83.4% in AR4. We attribute the large step increase from AR1 to AR2 to a change in flow regime present in the aneurysms. In AR1, we observe a momentum-driven regime which washes out high resident cells with each pulse, whereas the shear-driven regimes of AR2, AR3 and AR4

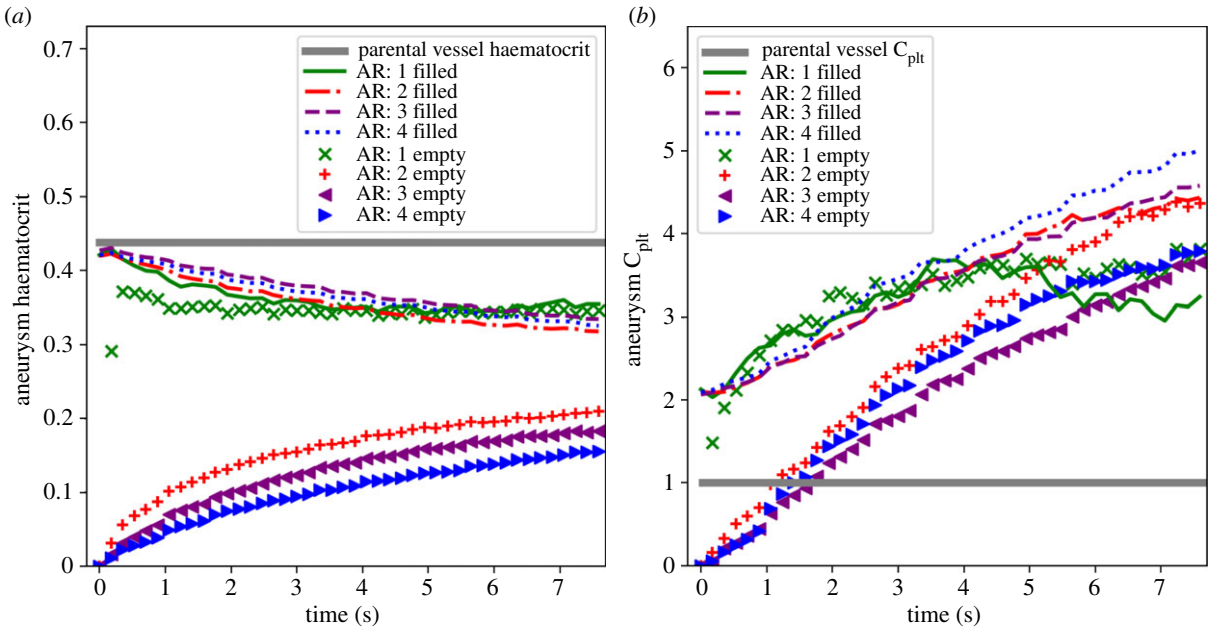

Figure 3. Time evolution of the cell volume fractions in the aneurysms over all aspect ratios and initializations. (*a*) RBCs and (*b*) platelets, each cell volume fraction is normalized to the parental vessel value. AR1 is shown in green (crosses indicate empty and the dotted solid line indicates filled initial conditions (I.C.s)), AR2 is red (plus symbols indicate empty and the dot-dash line indicates filled I.C.s), AR3 is purple (left triangles indicate empty and the dashed line indicates filled I.C.s) and AR4 is blue (right triangles indicate empty and the dotted line indicates filled I.C.s). Parental cell volume fractions of each cell type shown as solid grey line in *a* and *b*. (Online version in colour.)

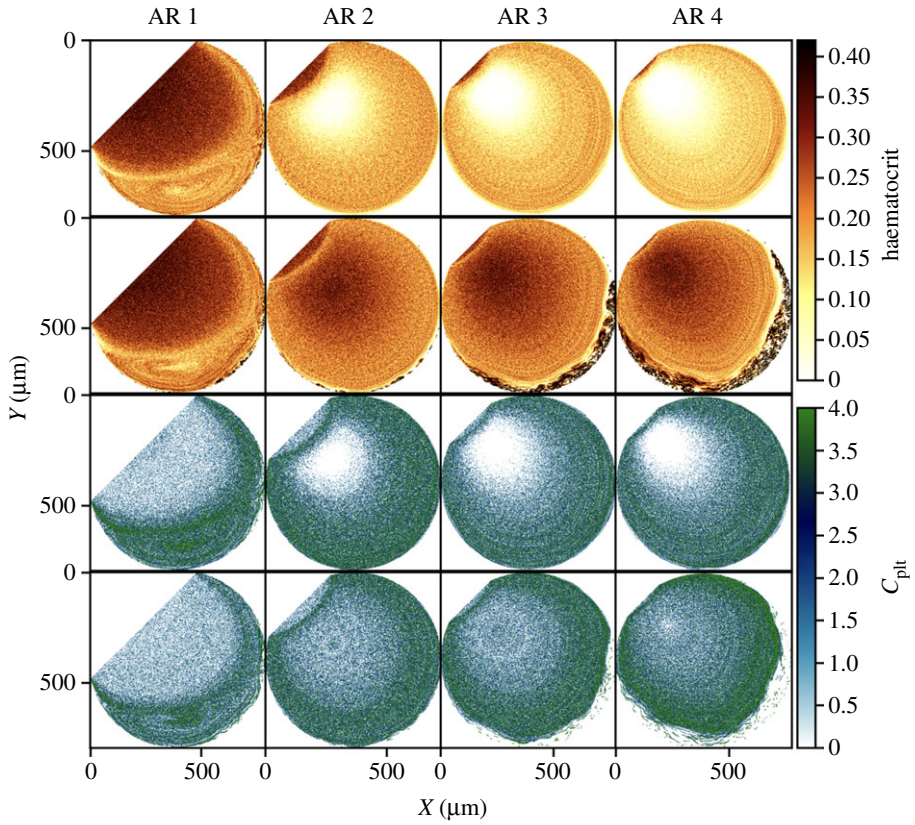

Figure 4. Aneurysm volume fractions for both filled and empty initial conditions along all aspect ratios (AR1,2,3,4). The top two rows are the haematocrit (coloured yellow-brown), the first row is the empty initialization and the second row is the filled initialization. The bottom two rows are the platelet volume fractions (coloured blue-green), the third row is the empty initialization and the fourth row is the filled initialization. Values are averaged over the final heartbeat and normalized to each cell type's parental vessel volume fraction.

show no significant washing out of high resident cells. This effect is independent of initialization, highlighted by the inset bar plot in figure 6, and is evident for both RBCs and platelets.

The AR1 case exhibits a layering of high and low residence cells of both RBCs and platelets within the recirculation zone, shown in the third and fourth rows of figure 5. We observe

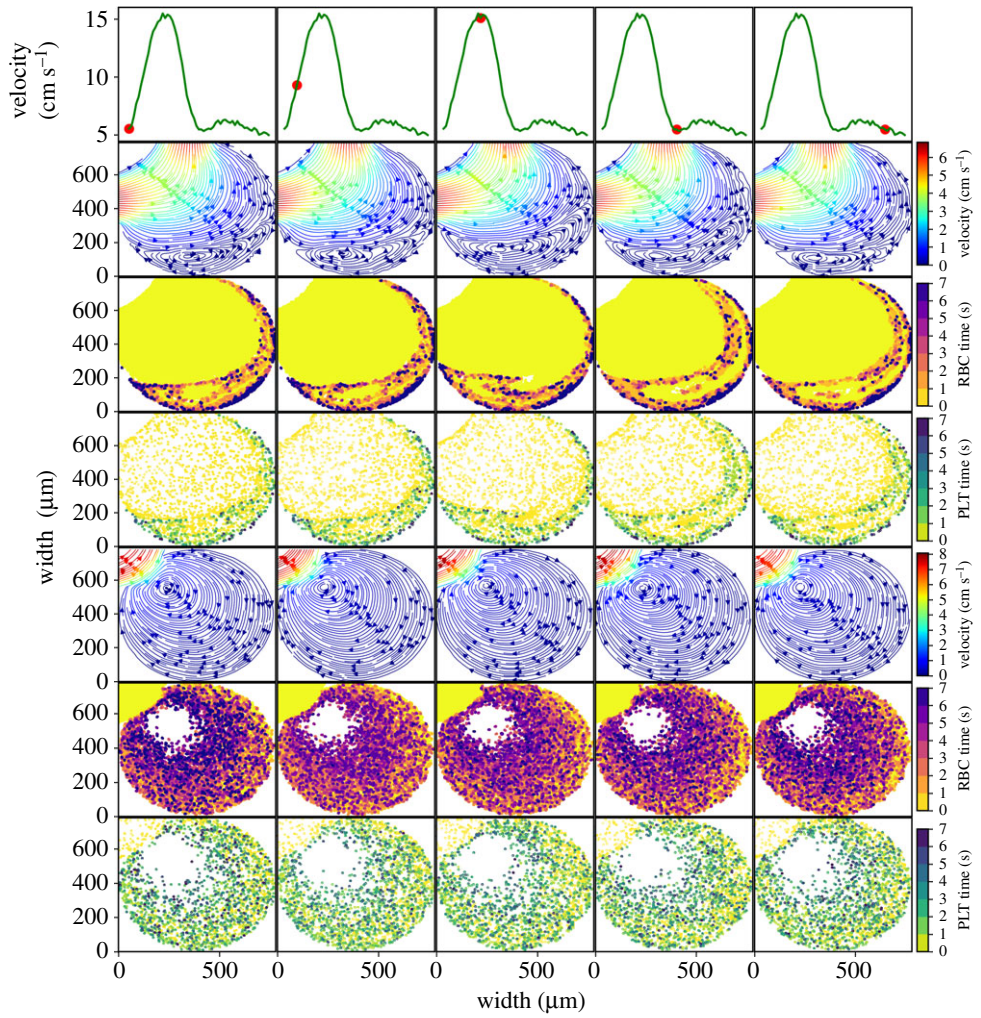

Figure 5. Time series of last heart cycle of the momentum-driven regime (AR1) and the shear-driven regime (AR3). The top row highlights the computed mean velocity of the parental vessel at five time points along the heart cycle. The AR1 aneurysm is shown in rows 2-4, with velocity stream lines in row 2 (coloured by magnitude), RBC residence times in row 3 (coloured yellow to purple) and platelet times (denoted PLT) in row 4 (coloured yellow to dark green). The AR3 aneurysm follows the same format and is shown in rows 5-7.

Table 1. Final aneurysm RBC and platelet volume fractions of both empty and filled initializations.

AR	haematocrit (empty)	haematocrit (filled)	C_{plt} (empty)	C_{plt} (filled)
1	0.34	0.35	0.0082	0.0069
2	0.21	0.32	0.0093	0.0094
3	0.18	0.33	0.0079	0.0096
4	0.16	0.32	0.0079	0.0096

with each heart cycle a layer of new cells that is injected into the recirculation zone and a population of high residence cells that are washed out. In the shear-driven case, cells with large residence times are well mixed in the aneurysm with no clear layering, with a tendency of moving towards the centre of the sac as they age. An example is shown from AR3 in the bottom two rows of figure 5.

3.4. Effect of pulsatility

We compared pulsatile flow to steady flow by rerunning all experiments with a steady Poiseuille flow profile with a mean parental velocity of 7.8 cm s^{-1}. This matches the mean parental velocity that is averaged over all heart cycles during the pulsatile simulations. In the steady flow cases, we observe all of the same results as we did with the pulsatile case: the same flow regimes in all aspect ratios, the same increasing trend of high resident cells with increasing aspect ratio. However, we do see that steady flow yields a larger high resident population in the the AR1 geometry compared to pulsatile flow (figure 7). This is true for both RBCs and platelets. This effect is not significant for the shear driven regime, i.e. AR2, AR3 and AR4. The variation in velocity through a heart cycle inside the aneurysm of the pulsatile case may lead to increased washing out of high resident cells from the aneurysm and therefore smaller trapped cell populations are produced. We do not see multiple vertices develop in the shear-driven steady flow case, and do not see clear influence of pulsatile flow.

4. Discussion

In this study, we examined the effect of pulsatility and aspect ratio on the transport of RBCs and platelets into simple two-dimensional sidewall saccular aneurysms. We find that both RBCs and platelets become increasingly trapped as the aspect ratio increases with a large jump of trapped cells going from

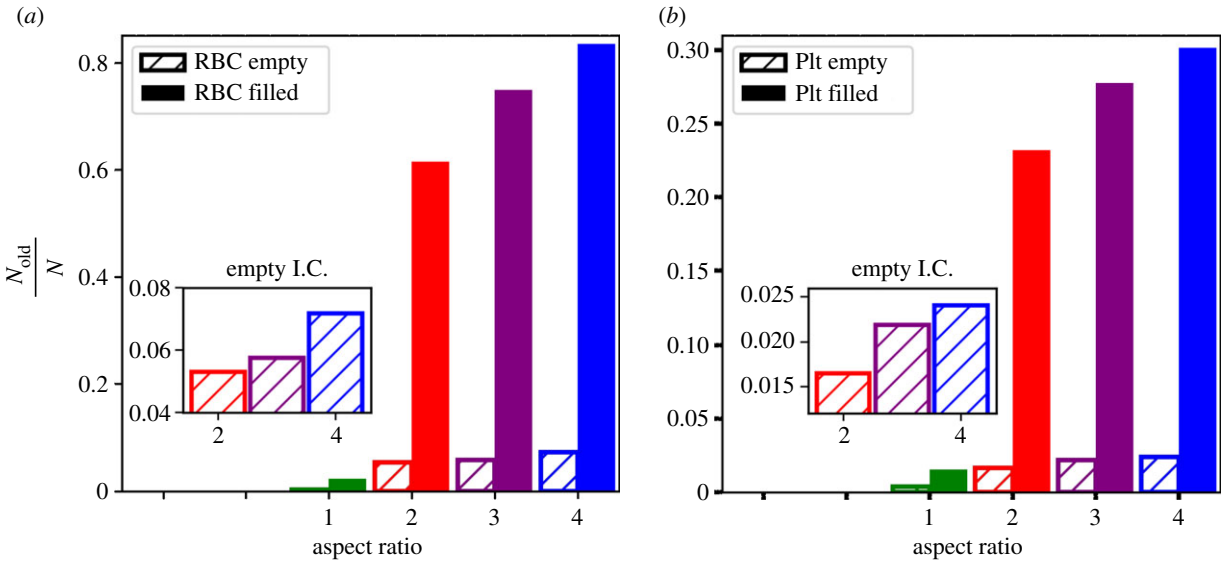

Figure 6. Ratio of high resident cells (residence times greater than or equal to 7 s) in each of the aneurysms (denoted N_{old}/N) for both initializations as a function of aspect ratio. (*a*) RBCs and (*b*) platelets. The filled initialization is shown as the main result in *a* and *b*, with the empty initialization is shown in *a* and *b* as an inset. (Online version in colour.)

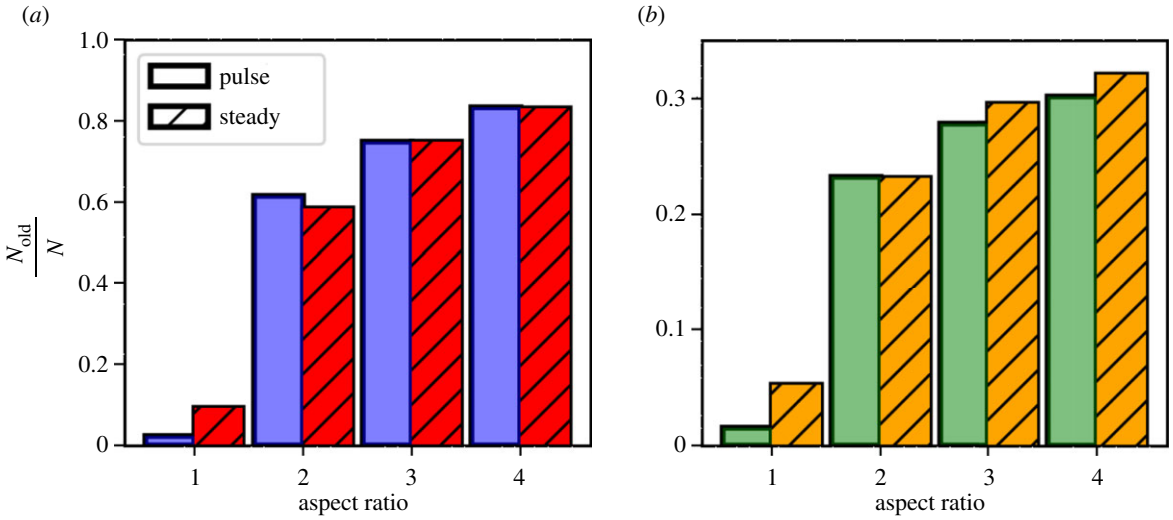

Figure 7. Comparison of the ratio of high residence cells (residence times greater than or equal to 7 s denoted N_{old}/N) in pulsatile flow versus steady flow as a function of aspect ratio. (*a*) RBCs and (*b*) platelets. Pulsatile flow is shown by the clear bars (blue for RBCS and green for platelets). Steady flow is shown by the hashed bars (red for RBCs and yellow for platelets). (Online version in colour.)

the aspect ratio 1–2. We attribute this large jump to a flow regime change from momentum driven with an inflow jet breakdown inside the aneurysm geometry to a shear regime where there is a continuous inflow jet. This jump in trapped cells over aspect ratio is similar to the findings of a percentage of clotted aneurysm volume from [24]. In this study, the jump is later in the aspect ratio, approximately from 2 to 4, where we observe the jump from 1 to 2. We think that this difference is highly dependent on the particular geometry. Also as the aspect ratio increases average aneurysm velocity decreases. Together with a higher old cell population, we can infer that aneurysms with higher aspect ratios are likely to be more thrombogenic.

Residence times of massless tracer particles are typically used in continuous CFD simulations to infer the locations where particle depositions may take place to form a thrombus [53,54]. These methods are limited as they only follow the flow lines and do not properly model the cellular nature and transport properties of whole blood. In this study, we are able to see a layering of old and new RBCs and platelets inside the recirculation zone of AR1. Aneurysms in our study are red blood cell-poor and platelet-rich compared to their parental vessel populations.

We observe that pulsatile flow will affect the population of high residence cells depending on the flow regime present in the aneurysm. In the momentum-driven regime of aspect ratio 1, we observe a lower population of high residence cells compared to the steady flow case. In the shear-driven regime of AR2, AR3 and AR4, we see no significant effect of pulsatility.

We initialized each simulation both uniformly filled with cells and empty of cells. Both initializations of AR1 reach the same haematocrit state within the first heart cycle, this is due to the momentum-driven regime present in this geometry where cells are immediately washed into and fill up the aneurysms with each pulse. The shear-driven aneurysms (AR2, AR3 and AR4) exhibit an inverse exponential growth in haematocrit if initialized empty of cells and an inverse exponential decay in haematocrit if initialized filled with cells. This slow change in aneurysm haematocrit state can be attributed to slowing

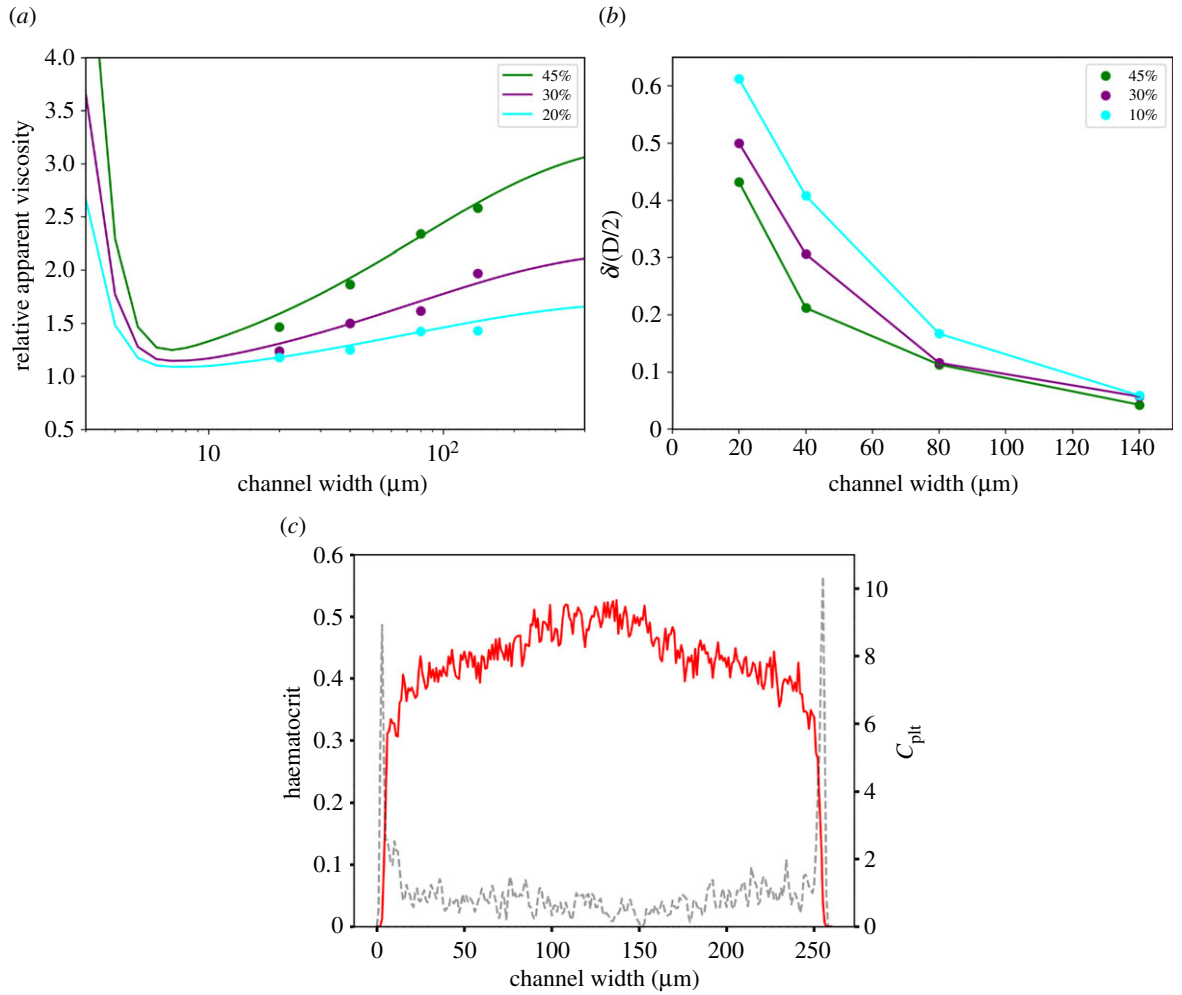

Figure 8. (*a*) Relative apparent viscosity as a function of vessel diameter at varying discharge haematocrits of 20, 30 and 45%. Empirical viscosity is plotted as lines from [57]. (*b*) The dimensionless cell free layer thickness as a function of vessel diameter and discharge haematocrit. (*c*) Haematocrit and platelet concentration (C_{plt}) profile in parental vessel of the AR2 geometry.

down of diffusion of RBCs from the wall to the centre of the aneurysms as shear rates decrease from the aneurysm wall to the centre of the aneurysm sac. The two initializations differ in final haematocrit states of the shear-driven regimes. However, we believe the trends shown in this paper will not change if we extend each simulation to or beyond 22 s. The trapped cell populations (figures 6 and 7) the flow regimes (figure 5) and the velocity decrease as the aspect ratio increases (figure 2) will continue to have the same trends if the simulations are extended.

These two-dimensional simulations are useful as they provide a systematic sweep, at a reasonable computational cost, over aspect ratios and can help narrow the cases to study with full three-dimensional cell-resolved models. In two dimensions, however, we are limited to resolve only the major in-plane inflow properties of the aneurysms like the continuous inflow jet and the inflow jet breakdown observed in this study. Vorticity dynamics presented in this study can be different from a three-dimensional case, patient specific or otherwise. In two dimensions, we observed diffusive transport of RBCs and platelets into the aneurysms of AR2, AR3 and AR4, while in three dimensions the diffusive transport may be much faster due to out-of-plane flow fields. We anticipate that this can affect the high residence populations as a function of aspect ratio presented in this study.

This study presents the transport of RBCs and platelets into aneurysm geometries which can add a better resolution to residence times as the methods used in this paper can resolve the fluid interaction with the suspended cells. Typically this is left out with the use of massless tracer particles which only follow stream lines and do not interact with the fluid. Wall shear stress is an important property that cell-resolved simulations can help to recover more accurately for simulation studies for aneurysms. With cell-resolved simulations, the viscosity is not constant and in reality depends on both the local haematocrit and local shear. With the methods presented in this paper, one can resolve a variation of viscosity near the arterial wall due to the development of a cell-free layer. This will lead to a more accurate calculation of the wall shear stress used in flow studies in aneurysms.

Data accessibility. The software used in this research, HemoCell2D, is available from the public git repository https://gitlab.computationalscience.nl/CSL/HemoCell2D. Each aspect ratio and validation case is available on this repository. Data from the simulations are available upon request.

Authors' contributions. B.C. conceived and designed this study, performed the analysis and wrote the paper. G.Z. conceived this study and provided scientific advice, specifically concerning the aneurysms and related haemodynamics. V.A. implemented the boundary conditions in HemoCell2D and provided technical support. A.G.H. conceived and supervised this research. All authors edited the manuscript and gave the final approval for the publication.

Competing interests. We declare we have no competing interests.

Funding. Financial support was provided by the European Union Horizon 2020 research and innovation programme under grant

agreement no. 675451, the CompBioMed project. This work was sponsored by NWO Exacte Wetenschappen (Physical Sciences) for the use of Lisa and Cartesius of the SURFsara high performance computing centre, with financial support from the Nederlandse Organisatie voor Wetenschappelijk Onderzoek (Netherlands Organization for Science Research, NWO).

Acknowledgements. We thank Sven Hirsch for a private conversation on the perspective of performing cell-resolved simulations in two dimensions. We also thank the research group of H.A. Marquering for their conversations regarding simulations of haemodynamics in aneurysms.

Appendix A

A.1. Validation

Blood plasma is simulated using the D2Q9 LBGK scheme [17] where the RBCs are deformable membranes represented by LSPs that are governed through a DEM force model. The LBM fluid and the DEM force model are coupled via the immersed boundary method. In this paper, we use a plasma dynamic viscosity of $\mu = 1.29$ mPa, which results from a kinematic plasma viscosity of $1.26 \times 10^{-7}\,\mathrm{m\,s^{-1}}$ and plasma density of $1025\,\mathrm{kg\,m^{-3}}$. We chose this as it is close to physiological values [55,56]. However, as this is a lower viscosity than the previously validated model, we rescale the coefficients of the force model by the same factor of the reduction of the plasma viscosity and re-validate the model. The force coefficients and relevant parameters of the two-dimensional model are shown in table 2. The DEM membrane model for the RBCs consists of four separate forces.

(i) A Hookean spring force acting between connecting LSP points to represent stretching and compression of the RBC.

$$\mathbf{F}_{\mathrm{spr}} = -C_{\mathrm{spr}}(|\mathbf{r}_{i+1} - \mathbf{r}_i| - r_0)\mathbf{e}_{i,i+1}. \tag{A 1}$$

Here, r_0 is the equilibrium spring length, $\mathbf{e}_{i,i+1}$ is the unit vector connecting the two LSP points, and C_{spr} is the spring constant.

(ii) A bending resistance force acting on two neighbouring LSP points.

$$\left.\begin{aligned} \mathbf{F}_{\mathrm{trs}} &= -f_{\mathrm{trs}}\mathbf{n}_i \\ \text{and}\quad f_{\mathrm{trs}} &= -C_{\mathrm{trs}}((\mathbf{r}_i - \mathbf{r}_{i-1}) \cdot (\mathbf{r}_{i+1} - \mathbf{r}_i)). \end{aligned}\right\} \tag{A 2}$$

Here, $\mathbf{n}_i$ is the normal vector of the LSP point resulting from the angle between $\mathbf{r}_i$ and $\mathbf{r}_{i+1}$. f_{trs} is the magnitude of the force which depends on the bending force constant C_{trs} and the angles between neighbouring LSP points r_i and r_{i+1}.

(iii) An area conservation force. Owing to the discretization of the cell, the total force may not be zero. To maintain an equilibrium cell volume (area in two dimensions), a relaxation mechanism is applied to correct for this non-zero total force.

$$\mathbf{F}_{\mathrm{area}} = -C_{\mathrm{area}}(A - A_0)\mathbf{n}_i. \tag{A 3}$$

Here, A_0 is the equilibrium cell area with C_{area} being the area force constant.

(iv) A repulsive force to prevent cells from sticking due to overlap of the IBM kernels and helps tune the emerging rheology of the suspension.

$$\mathbf{F}_{\mathrm{rep}} = -C_{\mathrm{rep}}(h^{-2})\mathbf{e}_{i,j}, \quad h \geq h_{\mathrm{cutoff}}. \tag{A 4}$$

Here, C_{rep} is the repulsion force constant, $\mathbf{e}_{ij}$ is the unit vector of two LSP points of two difference cells. h_{cutoff} is the threshold distance to ensure the repulsive force acts only if the two LSP points r_i and r_j are close enough to interact, otherwise $h_{\mathrm{cutoff}} = 0$ which results in a force that is zero.

Table 2. Model parameters and constants.

parameter	value
plasma density, ρ	$1025\,\mathrm{kg\,m^{-3}}$
kinematic viscosity, η	$1.26 \times 10^{-7}\,\mathrm{m^2\,s^{-1}}$
no. LSPs per RBC	26
no. LSPs per platelet	8
spring constant, C_{spr}	$0.37 \times 10^{-3}\,\mathrm{N\,m^{-1}}$
bending constant, C_{trs}	$0.74 \times 10^{-9}\,\mathrm{N\,rad^{-1}}$
area constant, C_{area}	$7.25 \times 10^{4}\,\mathrm{N\,m^{-2}}$
cell–cell constant, C_{rep}	$1.35 \times 10^{-22}\,\mathrm{Nm^2}$
cut-off distance, h_{cutoff}	0.6 lattice units
LBM relaxation constant, τ	1.1
spatial resolution, Δx	1 μm
time step, Δt	1.5×10^{-7} s

RBCs following this model are initialized as discs but are deflated to an equilibrium shape following an area ratio $A_{\mathrm{rbc}}/A_{\mathrm{sphere}} = 0.45$. This area ratio and the DEM model ensures that the equilibrium shape of the RBC is biconcave. The description of the IBM kernel used to couple the DEM method to the LBM fluid is omitted because we use exactly the same kernel employed for the initial validation of this model [30]. With this model, using scaled force coefficients and plasma viscosity, we are able to reproduce the Fåhraeus–Lindqvist effect, figure 8*a*, and the existence of a cell free layer and its decrease in thickness with an increase of vessel diameter, figure 8*b*.

The Fåhraeus–Lindqvist is the decrease of the apparent viscosity of whole blood as blood vessel size decreases [58]. An empirical relationship of this effect has been derived from a comprehensive database of *in vitro* measurements [57]. Our model shows good agreement with the apparent viscosity curves of Pries, as shown in figure 8*a*. We reproduce this effect over discharge haematocrits of $H_{\mathrm{d}} = 20$, 30, and 45% in straight vessels of a diameter range of 20–140 μm. We follow the Pries validation methods used by Bagchi [59]. The results are averaged over 0.1 s, which we found to be sufficient to converge to a stable apparent viscosity value. In our simulations, like Bagchi, we found that μ_{rel} is sensitive to U_{mean}, the mean flow velocity in our tubes, and the actual number of simulations performed is much greater than the points shown.

The thickness of the cell free layer is dependent on haematocrit and vessel size. Shown in figure 8*b* is the decrease of dimensionless thickness of the CFL as the vessel size increases. We calculate the cell free layer as a number density distribution across the diameter of the vessel. Our method of calculating the CFL is based on Bagchi [59], Durlofky & Brady [60] and Zhou & Pozrikidis [61]. Here, we take horizontal segments of 1 μm in width across the entire diameter and count the number of LSP of each cell type within that segment. We assume that each LSP carries an equal fraction of the total surface area of each RBC.

A.2. Computational resources

The simulation code used in this project, HemoCell2D, has been parallelized using MPI allowing efficient running of simulations using hundreds of compute cores. Linear scaling of the total runtime with the inverse number of processors has been shown up to 256 processors. The computational resources used for each simulation, time series shown in figure 3, were 160 compute cores over a wall time of approximately 5 days and 12 h. This includes the integration of 853 218 LBM fluid nodes, 21 628 RBCs and 3008 platelets (values reported from the last time point of the AR1 filled simulation) in both pre-inlet and flow domains. For further details on the performance of the code please, refer to the website https://www.hemocell.eu/hemocell2d/.

References

1. Rinkel GJE, Djibuti M, Algra A, van Gijn J. 1998 Prevalence and risk of rupture of intracranial aneurysms. *Stroke* **29**, 251–256. (doi:10.1161/01.STR.29.1.251)
2. Linn FHH, Rinkel GJE, Algra A, Van Gijn J. 1996 Incidence of subarachnoid hemorrhage. *Stroke* **27**, 625–629. (doi:10.1161/01.STR.27.4.625)
3. Weir B. 2002 Unruptured intracranial aneurysms: a review. *J. Neurosurg.* **96**, 3–42. (doi:10.3171/jns.2002.96.1.0003)
4. Brownlee RD, Tranmer BI, Sevick RJ, Karmy G, Curry BJ. 1995 Spontaneous thrombosis of an unruptured anterior communicating artery aneurysm. *Stroke* **26**, 1945–1949. (doi:10.1161/01.STR.26.10.1945)
5. Steinman DA, Milner JS, Norley CJ, Lownie SP, Holdsworth DW. 2003 Image-based computational simulation of flow dynamics in a giant intracranial aneurysm. *AJNR Am. J. Neuroradiol.* **24**, 559–566.
6. Hassan T, Ezura M, Timofeev EV, Tominaga T, Saito T, Takahashi A, Takayama K, Yoshimoto T. 2004 Computational simulation of therapeutic parent artery occlusion to treat giant vertebrobasilar aneurysm. *AJNR Am. J. Neuroradiol.* **25**, 63–68.
7. Cebral JR, Castro MA, Burgess JE, Pergolizzi RS, Sheridan MJ, Putman CM. 2005 Characterization of cerebral aneurysms for assessing risk of rupture by using patient-specific computational hemodynamics models. *AJNR Am. J. Neuroradiol.* **26**, 2550–2559.
8. Závodszky G, Paál G. 2013 Validation of a lattice Boltzmann method implementation for a 3D transient fluid flow in an intracranial aneurysm geometry. *Int. J. Heat Fluid Flow* **44**, 276–283. (doi:10.1016/j.ijheatfluidflow.2013.06.008)
9. Oeltze-Jafra S, Cebral JR, Janiga G, Preim B. 2016 Cluster analysis of vortical flow in simulations of cerebral aneurysm hemodynamics. *IEEE Trans. Vis. Comput. Graph.* **22**, 757–766. (doi:10.1109/TVCG.2015.2467203)
10. Varble N, Trylesinski G, Xiang J, Snyder K, Meng H. 2017 Identification of vortex structures in a cohort of 204 intracranial aneurysms. *J. R. Soc. Interface* **14**, 20170021. (doi:10.1098/rsif.2017.0021)
11. Schneiders JJ *et al.* 2015 Additional value of intra-aneurysmal hemodynamics in discriminating ruptured versus unruptured intracranial aneurysms. *AJNR Am. J. Neuroradiol.* **36**, 1920–1926. (doi:10.3174/ajnr.A4397)
12. Basombrío FG, Dari EA, Buscaglia GC, Feijóo RA. 2002 Numerical experiments in complex haemodynamic flows. Non-newtonian effects. *Int. J. Comut. Fluid Dyn.* **16**, 231–246. (doi:10.1080/1061856021000025111)
13. Cebral JR, Adrián Castro M, Appanaboyina S, Putman CM, Millan D, Frangi AF. 2005 Efficient pipeline for image-based patient-specific analysis of cerebral aneurysm hemodynamics: technique and sensitivity. *IEEE Trans. Med. Imaging* **24**, 457–467. (doi:10.1109/TMI.2005.844159)
14. Moore S, David T, Chase JG, Arnold J, Fink J. 2006 3D models of blood flow in the cerebral vasculature. *J. Biomech.* **39**, 1454–1463. (doi:10.1016/j.jbiomech.2005.04.005)
15. Kim CS, Kiris C, Kwak D, David T. 2006 Numerical simulation of local blood flow in the carotid and cerebral arteries under altered gravity. *J. Biomech. Eng.* **128**, 194–202. (doi:10.1115/1.2165691)
16. Bernsdorf J, Wang D. 2009 Non-newtonian blood flow simulation in cerebral aneurysms. *Comput. Math. Appl.* **58**, 1024–1029. (doi:10.1016/j.camwa.2009.02.019)
17. Succi S. 2001 *The lattice Boltzmann equation: for fluid dynamics and beyond*. Oxford, UK: Oxford university press.
18. Krüger T, Kusumaatmaja H, Kuzmin A, Shardt O, Silva G, Magnus Viggen E. 2017 *The lattice Boltzmann method*. Berlin, Germany: Springer.
19. Ouared R, Chopard B. 2005 Lattice Boltzmann simulations of blood flow: non-newtonian rheology and clotting processes. *J. Stat. Phys.* **121**, 209–221. (doi:10.1007/s10955-005-8415-x)
20. Chopard B, Ouared R, Ruefenacht DA, Yilmaz H. 2007 Lattice Boltzmann modeling of thrombosis in giant aneurysms. *Int. J. Mod. Phys. C* **18**, 712–721. (doi:10.1142/S0129183107010978)
21. Chopard B, Ouared R, Rüfenacht DA. 2006 A lattice Boltzmann simulation of clotting in stented aneursysms and comparison with velocity or shear rate reductions. *Math. Comput. Simul.* **72**, 108–112. (doi:10.1016/j.matcom.2006.05.025)
22. Ouared R, Chopard B, Stahl B, Rüfenacht DA, Yilmaz H, Courbebaisse G. 2008 Thrombosis modeling in intracranial aneurysms: a lattice Boltzmann numerical algorithm. *Comput. Phys. Commun.* **179**, 128–131. (doi:10.1016/j.cpc.2008.01.021)
23. Malaspinas O *et al.* 2016 A spatio-temporal model for spontaneous thrombus formation in cerebral aneurysms. *J. Theor. Biol.* **394**, 68–76. (doi:10.1016/j.jtbi.2015.12.022)
24. Ribeiro de Sousa D *et al.* 2015 Determination of a shear rate threshold for thrombus formation in intracranial aneurysms. *J. Neurointerv. Surg.***8**, 853–858. (doi:10.1136/neurintsurg-2015-011737)
25. Pivkin IV, Em Karniadakis G. 2008 Accurate coarse-grained modeling of red blood cells. *Phys. Rev. Lett.* **101**, 118105. (doi:10.1103/PhysRevLett.101.118105)
26. Fedosov DA, Caswell B, Em Karniadakis G. 2010 Systematic coarse-graining of spectrin-level red blood cell models. *Comput. Methods Appl. Mech. Eng.* **199**, 1937–1948. (doi:10.1016/j.cma.2010.02.001)
27. Krüger T, Varnik F, Raabe D. 2011 Efficient and accurate simulations of deformable particles immersed in a fluid using a combined immersed boundary lattice Boltzmann finite element method. *Comput. Math. Appl.* **61**, 3485–3505. (doi:10.1016/j.camwa.2010.03.057)
28. Závodszky G, van Rooij B, Azizi V, Hoekstra A. 2017 Cellular level *in-silico* modeling of blood rheology with an improved material model for red blood cells. *Front. Physiol.* **8**, 563. (doi:10.3389/fphys.2017.00563)
29. Mountrakis L, Lorenz E, Hoekstra AG. 2013 Where do the platelets go? A simulation study of fully resolved blood flow through aneurysmal vessels. *Interface Focus* **3**, 20120089. (doi:10.1098/rsfs.2012.0089)
30. Mountrakis L, Lorenz E, Hoekstra AG. 2014 Validation of an efficient two-dimensional model for dense suspensions of red blood cells. *Int. J Mod. Phys. C* **25**, 1441005. (doi:10.1142/S0129183114410058)
31. Peskin CS. 2002 The immersed boundary method. *Acta Numer.* **11**, 479–517. (doi:10.1017/S0962492902000077)
32. Hassan T, Timofeev EV, Saito T, Shimizu H, Ezura M, Matsumoto Y, Takayama K, Tominaga T, Takahashi A. 2005 A proposed parent vessel geometry-based categorization of saccular intracranial aneurysms: computational flow dynamics analysis of the risk factors for lesion rupture. *J. Neurosurg.* **103**, 662–680. (doi:10.3171/jns.2005.103.4.0662)
33. Burleson AC, Strother CM, Turitto VT. 1995 Computer modeling of intracranial saccular and lateral aneurysms for the study of their hemodynamics. *Neurosurgery* **37**, 774–784. (doi:10.1227/00006123-199510000-00023)
34. Ujiie H, Tamano Y, Sasaki K, Hori T. 2001 Is the aspect ratio a reliable index for predicting the rupture of a saccular aneurysm? *Neurosurgery* **48**, 495–503. (doi:10.1097/00006123-200103000-00007)

35. Azizi Tarksalooyeh VW, Závodszky G, van Rooij BJM, Hoekstra AG. 2018 Inflow and outflow boundary conditions for 2D suspension simulations with the immersed boundary lattice Boltzmann method. *Comput. Fluids* **172**, 312–317. (doi:10.1016/j.compfluid.2018.04.025)
36. Zou Q, He X. 1997 On pressure and velocity boundary conditions for the lattice Boltzmann bgk model. *Phys. Fluids* **9**, 1591–1598. (doi:10.1063/1.869307)
37. Venugopal P, Valentino D, Schmitt H, Pablo Villablanca J, Viñuela F, Duckwiler G. 2007 Sensitivity of patient-specific numerical simulation of cerebal aneurysm hemodynamics to inflow boundary conditions. *J. Neurosurg.* **106**, 1051–1060. (doi:10.3171/jns.2007.106.6.1051)
38. Ugron Á, Paál G. 2014 On the boundary conditions of cerebral aneurysm simulations. *Periodica Polytechnica Mech. Eng.* **58**, 37–45. (doi:10.3311/PPme.7392)
39. Li Z, Kleinstreuer C. 2005 Fluid–structure interaction effects on sac-blood pressure and wall stress in a stented aneurysm. *J. Biomech. Eng.* **127**, 662–671. (doi:10.1115/1.1934040)
40. McGregor RHP, Szczerba D, Székely G. 2007 A multiphysics simulation of a healthy and a diseased abdominal aorta. In *Int. Conf. on Medical Image Computing and Computer-Assisted Intervention*, pp. 227–234. Berlin, Germany: Springer.
41. István Józsa T, Paál G. 2014 Boundary conditions for flow simulations of abdominal aortic aneurysms. *Int. J. Heat Fluid Flow* **50**, 342–351. (doi:10.1016/j.ijheatfluidflow.2014.09.004)
42. Salmon S, Thiriet M, Gerbeau J-F. 2003 Medical image-based computational model of pulsatile flow in saccular aneurisms. *ESAIM: Math. Modell. Numer. Anal.* **37**, 663–679. (doi:10.1051/m2an:2003053)
43. Quinn U, Tomlinson LA, Cockcroft JR. 2012 Arterial stiffness. *JRSM Cardiovasc. Dis.* **1**, 1–8. (doi:10.1258/cvd.2012.012024)
44. Womersley JR. 1957 The mathematical analysis of the arterial circulation in a state of oscillatory motion. Wright Air Development Center Technical Report WADC-TR-56-614.
45. AM Artoli, AG Hoekstra, PMA Sloot. 2002 Accuracy of 2D pulsatile flow in the lattice Boltzmann bgk method. In *Int. Conf. on Computational Science*, pp. 361–370. Berlin, Germany: Springer.
46. Bouvy WH, Geurts LJ, Kuijf HJ, Luijten PR, Kappelle LJ, Biessels GJ, Zwanenburg JJM. 2016 Assessment of blood flow velocity and pulsatility in cerebral perforating arteries with 7-T quantitative flow mri. *NMR Biomed.* **29**, 1295–1304. (doi:10.1002/nbm.3306)
47. Boron WF, Boulpaep EL. 2008 *Medical physiology*. Philadelphia, PA: Elsevier Health Sciences.
48. Björkman SE. 1959 A new method for enumeration of platelets. *Acta Haematol.* **22**, 377–379. (doi:10.1159/000205797)
49. Chodzyński KJ *et al.* 2016 Does the gravity orientation of saccular aneurysms influence hemodynamics? An experimental study with and without flow diverter stent. *J. Biomech.* **49**, 3808–3814. (doi:10.1016/j.jbiomech.2016.10.007)
50. Jan Tangelder G, Slaaf DW, Teirlinck HC, Alewijnse R, Reneman RS. 1982 Localization within a thin optical section of fluorescent blood platelets flowing in a microvessel. *Microvasc. Res.* **23**, 214–230. (doi:10.1016/0026-2862(82)90066-8)
51. Tilles AW, Eckstein EC. 1987 The near-wall excess of platelet-sized particles in blood flow: its dependence on hematocrit and wall shear rate. *Microvasc. Res.* **33**, 211–223. (doi:10.1016/0026-2862(87)90018-5)
52. Skorczewski T, Crowl Erickson L, Fogelson AL. 2013 Platelet motion near a vessel wall or thrombus surface in two-dimensional whole blood simulations. *Biophys. J.* **104**, 1764–1772. (doi:10.1016/j.bpj.2013.01.061)
53. Hardman D, Doyle BJ, Semple SIK, Richards JMJ, Newby DE, Easson WJ, Hoskins PR. 2013 On the prediction of monocyte deposition in abdominal aortic aneurysms using computational fluid dynamics. *Proc. Inst. Mech. Eng. H J. Eng. Med.* **227**, 1114–1124. (doi:10.1177/0954411913494319)
54. Rayz VL, Boussel L, Ge L, Leach JR, Martin AJ, Lawton MT, McCulloch C, Saloner D. 2010 Flow residence time and regions of intraluminal thrombus deposition in intracranial aneurysms. *Ann. Biomed. Eng.* **38**, 3058–3069. (doi:10.1007/s10439-010-0065-8)
55. Késmárky G, Kenyeres P, Rábai M, Tóth K. 2008 Plasma viscosity: a forgotten variable. *Clin. Hemorheol. Microcirc.* **39**, 243–246.
56. Brust M, Schaefer C, Doerr R, Pan L, Garcia M, Arratia PE, Wagner C. 2013 Rheology of human blood plasma: viscoelastic versus newtonian behavior. *Phys. Rev. Lett.* **110**, 078305. (doi:10.1103/PhysRevLett.110.078305)
57. Pries AR, Secomb TW, Gessner T, Sperandio MB, Gross JF, Gaehtgens P. 1994 Resistance to blood flow in microvessels *in vivo*. *Circ. Res.* **75**, 904–915. (doi:10.1161/01.RES.75.5.904)
58. Fåhræus R, Lindqvist T. 1931 The viscosity of the blood in narrow capillary tubes. *Am. J. Physiol. Legacy Content* **96**, 562–568. (doi:10.1152/ajplegacy.1931.96.3.562)
59. Bagchi P. 2007 Mesoscale simulation of blood flow in small vessels. *Biophys. J.* **92**, 1858–1877. (doi:10.1529/biophysj.106.095042)
60. Durlofsky LJ, Brady JF. 1989 Dynamic simulation of bounded suspensions of hydrodynamically interacting particles. *J. Fluid Mech.* **200**, 39–67. (doi:10.1017/S0022112089000558)
61. Zhou H, Pozrikidis C. 1993 The flow of ordered and random suspensions of two-dimensional drops in a channel. *J. Fluid Mech.* **255**, 103–127. (doi:10.1017/S0022112093002411)